EDGE ARTICLE

Check for updates

The first polyanion-substitution-driven centrosymmetric-to-noncentrosymmetric structural transformation realizing an excellent nonlinear optical supramolecule [Cd$_4$P$_2$][CdBr$_4$]†

Zhi-Xin Qiu,[a] Zhe-Xiong Zheng,[a] Xiao-Ming Jiang, [iD][ab] Bin-Wen Liu [iD] *[ab] and Guo-Cong Guo [iD] *[ab]

Crystallographically, noncentrosymmetricity (NCS) is an essential precondition and foundation of achieving nonlinear optical (NLO), pyroelectric, ferroelectric, and piezoelectric materials. Herein, structurally, octahedral [SmCl$_6$]$^{3-}$ is substituted by the acentric tetrahedral polyanion [CdBr$_4$]$^{2-}$, which is employed as a templating agent to induce centrosymmetric (CS)-to-NCS transformation based on the new CS supramolecule [Cd$_5$P$_2$][SmCl$_6$]Cl (**1**), thereby providing the NCS supramolecule [Cd$_4$P$_2$][CdBr$_4$] (**2**). Meanwhile, this replacement further results in the host 2D $_\infty^2$[Cd$_5$P$_2$]$^{4+}$ layers converting to yield the twisted 3D $_\infty^3$[Cd$_4$P$_2$]$^{2+}$ framework, which promotes the growth of bulk crystals. Additionally, phase **2** possesses well-balanced NLO properties, enabling considerable second-harmonic generation (SHG) responses (0.8–2.7 × AgGaS$_2$) in broadband spectra, the thermal expansion anisotropy (2.30) together with suitable band gap (2.37 eV) primarily leading to the favorable laser-induced damage threshold (3.33 × AgGaS$_2$), broad transparent window, and sufficient calculated birefringence (0.0433) for phase-matching ability. Furthermore, the first polyanion substitution of the supramolecule plays the role of templating agent to realize the CS-to-NCS transformation, which offers an effective method to rationally design promising NCS-based functional materials.

Introduction

A noncentrosymmetric (NCS) crystallographic structure is an essential prerequisite for symmetry-dependent properties, such as pyroelectric, ferroelectric, piezoelectric, and second-order nonlinear optical (NLO) materials.[1–3] After considering the structural characteristics, practical strategies have been put forth for creating NCS materials, which can commonly be classified into the following categories. Primarily, NCS crystals can be synthesized using basic structural and functional motifs,[4] including distorted polyhedrons centered by second-order Jahn–Teller effects or stereochemically active lone pair cations, asymmetrical tetrahedral units, and plane-trigonal π-orbital systems. These polyhedrons have been applied to significantly increase the possibilities for producing NCS compounds, such as Cs$_4$V$_8$O$_{22}$,[5] Pb$_2$GaF$_2$(SeO$_3$)$_2$Cl,[6]

BaF$_2$TeF$_2$(OH)$_2$,[7] Rb$_3$VO(O$_2$)$_2$CO$_3$,[8] RbMgCO$_3$F,[9] CsAlB$_3$O$_6$F,[10] NaAsS$_2$,[11] Eu$_2$P$_2$S$_6$,[12] Li$_2$CdGeS$_4$,[13] BaHgSe$_2$,[14] SrCdSiS$_4$,[15] and Li$_4$CdSn$_2$S$_7$.[16] Moreover, it is worth mentioning that chemical substitution serves as a highly effective alternative pathway for synthesizing NCS compounds. For example, an NCS oxide Ba$_2$-NaClP$_2$O$_7$ that manifested excellent optical performance was derived from the multiple-site substitution of fresnoite-type structure Ba$_2$TiOSi$_2$O$_7$;[17] recently, NCS salt-inclusion chalcogenide was derived by employing a polycation-substitution-induced strategy and exhibited outstanding NLO performances;[18] lately, a ternary deficient Cd$_3$PI$_3$ diamond-like structure was transformed by anionic aliovalent substitution using NCS ZnS as a template.[19] On the whole, the probability of crystalizing in NCS structure is always considerably lower than in CS structure; therefore, a feasible approach for the further oriented synthesis of NCS compounds remains a major challenge. Therein, the strategy of CS-to-NCS structural transformation has been confirmed to effectively create NCS material systems.[20] Nevertheless, an inorganic compound with polyanion-substitution-driven CS-to-NCS structural transformation has yet to be reported.

Owing to their frequency conversion capabilities, NLO crystalline materials have an irreplaceable role in solid-state laser efficiently generating coherent beams.[21–27] As potential IR NLO

[a]State Key Laboratory of Structural Chemistry, Fujian Institute of Research on the Structure of Matter, Chinese Academy of Sciences, Fuzhou, Fujian, 350002, P. R. China. E-mail: bwliu@fjirsm.ac.cn; gcguo@fjirsm.ac.cn

[b]Fujian Science & Technology Innovation Laboratory for Opto-Electronic Information of China, Fuzhou, Fujian 350108, P. R. China

† Electronic supplementary information (ESI) available. CCDC 2235035 and 2235036. For ESI and crystallographic data in CIF or other electronic format see DOI: https://doi.org/10.1039/d3sc04818g

candidates, supramolecular pnictide halides constructed from host and guest lattice frameworks have the unique characteristics of adjustable functional motifs for structural diversity and flexible properties.[28] Therefore, exploring an expected NCS pnictide halide as an ideal IR NLO material is urgently needed. Structurally, the guest motifs of the supermolecule, particularly distorted polyhedrons such as acentric tetrahedral units, often act as NCS templates to construct the host–guest framework. Taking the above into consideration, the octahedral $[SmCl_6]^{3-}$ unit in CS supramolecular $[Cd_5P_2][SmCl_6]Cl$ (1) is substituted with acentric tetrahedral $[CdBr_4]^{2-}$ by applying the polyanion-substitution-driven transformation strategy, offering a CS-to-NCS compound $[Cd_4P_2][CdBr_4]$ (2). Notably, to the best of our knowledge, this is the first polyanion-substitution-driven CS-to-NCS transition of a supramolecule to be realized. Meanwhile, this substitution induces the angles of neighboring host layers to rotate by 120° and prompts the cationic layered $_\infty^2[Cd_5P_2]^{4+}$ to build the 3D $_\infty^3[Cd_4P_2]^{2+}$ framework. Moreover, compound 2 manifests balanced optical performance, including a significant SHG response, and a wide band gap as well as thermal expansion anisotropy for considerable LIDT.

Results and discussion

Single-crystal X-ray diffraction (XRD) analysis revealed that compound 1 crystallizes in the CS trigonal space group $P\text{-}3$ (No. 147, Table S1†) with cell lattice $a = b = 13.350$ (4) Å, $c = 7.308$ (4) Å, and $V = 1128.0(9)$ Å^3. The compound features a host–guest frame that opens the host $[Cd_5P_2]^{4+}$ tunneled framework running along the c-axis, wherein the discrete guest $[SmCl_6]^{3-}$ anions are embedded in the channels (Fig. 1a), and the remaining Cl atoms are fixed by ionic bonding of the Sm atoms with an equal bond length of 2.787 Å (Tables S2 and S3†). Each P atom in the host structure is tetrahedrally coordinated by Cd

atoms to establish the slightly distorted $[PCd_4]$ tetrahedron with bond distances of 2.420–2.430 Å. Six tetrahedral $[PCd_4]$ units are interconnected "hand by hand" to generate a $[P_6Cd_{18}]^{18+}$ 12-membered ring, which is in turn linked by apex-sharing, thus creating the $_\infty^2[Cd_5P_2]^{4+}$ cationic layers, as illustrated in Fig. 1b. In the guest structure formed by coordinating a split Sm atom with six Cl atoms, $[SmCl_6]^{3-}$ octahedra provide the covalent bond length of 2.417–2.688 Å. Compound 2 adopts NCS space group $Pna2_1$ (no. 33, Table S1†).[29] The structural feature consists of similar 12-membered rings $[P_6Cd_{18}]^{18+}$ connected by distorted tetrahedral $[PCd_4]$ units with a bond distance of 2.407–2.454 Å to form a similar tunnel-like cationic host framework. The pores are interspersed with infinite discontinuous guest acentric tetrahedral $[CdBr_4]^{2-}$ anions with a bond length of 2.540–2.720 Å (Fig. 1c). The layers consist of $[P_6Cd_{18}]^{18+}$ 12-membered rings that are further linked to each other to yield a 3D cationic $_\infty^3[Cd_4P_2]^{2+}$ framework running along the c-axis (Fig. 1d).

The octahedron $[SmCl_6]^{3-}$ template of 1 possesses a -3 symmetry inverted center operation, thereby causing the host moiety coordinated to the guest to become anti-parallel, thus resulting in the CS space group. The replacement of $[SmCl_6]^{3-}$ octahedron with acentric $[CdBr_4]^{2-}$ tetrahedron acting as the NCS template for the host–guest structure caused the symmetry to change by operating symmetrically in 2_1 spiral shafts to form the NCS structure. In brief, an effective polyanion-substitution modification method is applied to achieve the CS-to-NCS structural transformation, thereby breaking the symmetry of compound 1. This structural transformation can be expressed in detail by the dipole moment calculations.[30,31] As listed in Table S4,† the dipole moment calculations of compound 2 show that the observed dipole moment of the host–guest framework is cancelled out completely running down the x- and y-axes, whereas the dipole moment of the guest $[CdBr_4]^{2-}$ polyanion is 1.88 Debye in the direction of the z-axis. Under the influence of the guest polyanion, the dipole moments of the host $[PCd_4]^{5+}$ polycations add up to 26.64 Debye along the z-axis. This polar phenomenon indicates that the host–guest framework is arranged parallelly. Interestingly, distinguished from 1, the replacement of octahedrons with distorted tetrahedrons causes the angles between the adjacent host layers to rotate 120°, thereby resulting in the interlamellar spacing layer being connected by Cd–P chemical bonds to build the 3D framework of 2, which is a crucial parameter to ultimately achieve bulk single crystals.

Yellow crystals 1 and 2 with yields of 60% and 90%, respectively, were isolated after the products were repeatedly washed with deionized water. The energy-dispersive X-ray spectroscopy (EDS) analyses reveal the presence of elements of crystals 1 and 2 (Fig. S1†). The powder XRD patterns of samples 1 and 2 exhibited a well match with the calculated pattern obtained from single-crystal XRD analysis, indicating a high degree of certification (Fig. S2†). The UV-vis-NIR diffuse reflectance absorption spectra of compounds 1 and 2 generated from the Kubelka–Munk eqn (32) indicate that the band gap values are 2.60 and 2.37 eV (Fig. S3† and Fig. 2a), respectively, which correspond well to their yellow colors.[32] These results are
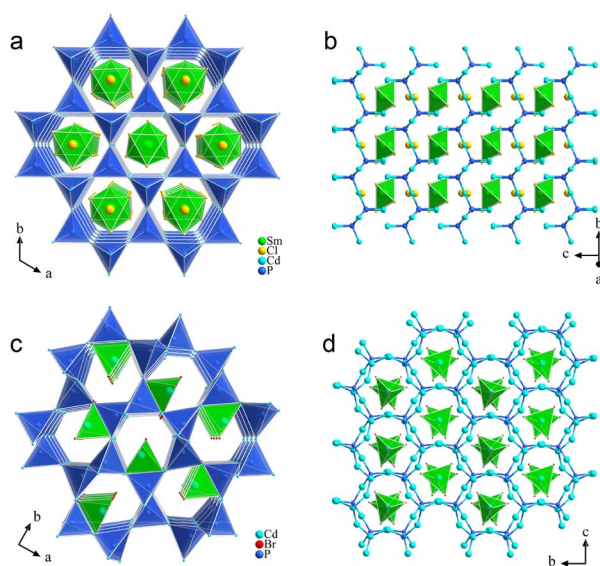

Fig. 1 Structures of compounds 1 (a) and 2 (c) are viewed along the c-axis, and the 3D framework of 2 (d) is built from the angles of the neighboring host layers in 1 (b) that is rotating 120° along the c-axis.
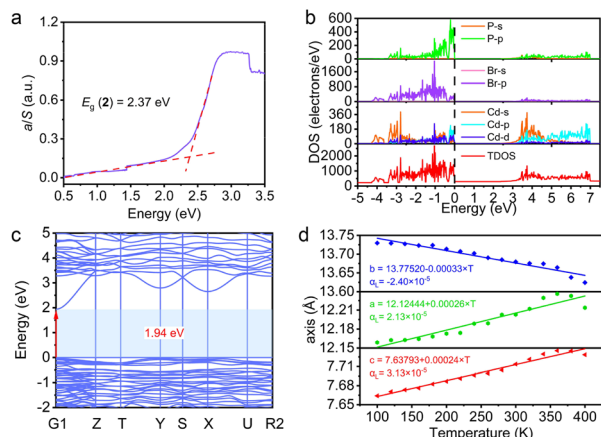
Fig. 2 (a) Band gap, (b) DOS, (c) electronic band structures, and (d) temperature-variation of the cell parameters of **2**.

broader than those of notable IR NLO materials $ZnGeP_2$ (1.8 eV)[33] and $AgGaSe_2$ (1.83 eV)[34], and comparable to those of supramolecules as demonstrated in $[Hg_6P_4Cl_3][PbCl_3]$ (2.29 eV)[35], $[Hg_{23}P_{12}][ZnCl_4]_6$ (2.30 eV)[36], and $[Hg_{11}P_4][GaCl_4]_4$ (2.42 eV)[37]. The electronic structures were calculated using density functional theory (DFT); compound **2** is a direct band gap semiconductor with a band gap of 1.94 eV (Fig. 2c, from G1 to G1)[38]. This discrepancy, where the calculated band gap is slightly smaller than the experimental value, can be attributed to the inadequate treatment of many-body correlations within the generalized gradient approximation. The calculated density of states (DOS) plot of **2** is illustrated in Fig. 2b, Br-4p and P-3p states dominantly constitute the maximum of valence bands; the Cd-5s and Cd-4p states display an immense contribution to the minimum of conduction bands, thereby demonstrating that the band gap of compound **2** is primarily determined by electronic transitions in the $[PCd_4]$ and $[CdBr_4]$ tetrahedrons.
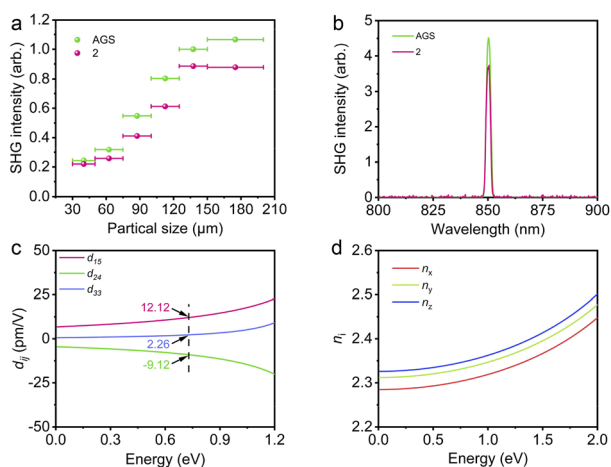

Fig. 3 (a) Phase-matching behavior of **2** at the incident laser of 1700 nm. (b) Comparison of the SHG signals of **2** and AGS at the same particle size of 150–200 μm. (c) Calculated frequency-dependent SHG coefficients of **2**. (d) Refractive indices of **2**.

A remarkable LIDT is one of the critical parameters for an NLO material to efficiently produce a high-power laser. The LIDT of **2** was performed by adjusting the laser output energy until the damage was observed under an optical microscope.[39] As listed in Table S5,† the LIDT of monocrystal **2** is 33.3 MW cm^{-2}, approximately 3.33 times that of commercial $AgGaS_2$ (AGS, 10.0 MW cm^{-2}) under the same measurement conditions. This value is comparable with other recently reported IR NLO crystals, such as $HgCuPS_4$ (4.2 × AGS)[40], $Pb_{13}O_6Cl_4Br_{10}$ (3.0 × AGS)[41], $Rb_{10}Zn_4$-Sn_4S_{17} (5.0 × AGS)[42], and $BaGe_2As_2$ (5.9 × AGS)[43]. Moreover, compound **2** manifests a band gap (2.37 eV) that avoids the one- and two-photon absorption at 2.09 μm. Furthermore, in terms of thermal properties, the thermal expansion coefficient (TEC) represents the capability of a crystal to withstand thermal shock under high-power laser irradiation. As illustrated in Fig. 2d, the corresponding TEC values (at × 10^{-5}) along the *a*-, *b*-, and *c*-axes of **2** are 2.13, −2.40, and 3.13, respectively. The thermal expansion anisotropy value (2.30) is relatively smaller than that of AGS (2.95)[44]. Therefore, the experimental observations demonstrate that the advantageous band gap and TEC lead to the LIDT enhancement, thereby making the crystal suitable for application in high-power lasers.

With the assistance of the modified Kurtz–Perry method,[45] we found that the SHG intensity of sample **2** was 2.7, 1.8, 1.9, 1.5, 1.1, 0.8, and 0.8 times that of benchmark AGS at broadband wavelengths from 1.06, 1.20, 1.30, 1.40, 1.50, 1.60, to 1.70 μm laser, respectively (Fig. S4†). Moreover, under an incident laser of 1.70 μm, the SHG intensity is positively correlated with the particle size and eventually tended to be horizontal, thereby illustrating phase-matchable attributes (Fig. 3a), and an SHG signal 0.8 times that of AGS is acquired (Fig. 3b). Therefrom, the effective SHG coefficient d_{eff}, calculated by the formula $d_{eff} = d_{eff,AGS} (I^{2\omega}/I^{2\omega}_{AGS})^{1/2}$ ($d_{eff,AGS} = 11.6$ pm V^{-1}), is determined to be 11.0 pm V^{-1}.[45] Such data is comparable with that recently reported for mixed-anion crystals $[Ba_2F_2][Ge_2O_3S_2]$ (1.4 × AGS)[46], $[KBa_4Cl][Ge_3S_{10}]$ (0.8 × AGS)[47], $SnI_4\cdot(S_8)_2$ (0.5 × AGS)[48], and $LaCaGaS_3O_7$ (0.9× AGS)[49]. Taking into account the point group *mm*2, the relevant calculation is carried out for its NLO property. There are three non-zero independent SHG coefficient tensors of **2** decided by Kleinman's symmetry constraint, and the values of the frequency-dependent tensors are considered at the measured wavelength of 0.73 eV, which are 12.12, 2.26, and −9.12 pm V^{-1} for d_{15}, d_{24}, and d_{33}, respectively (Fig. 3c). In addition, the calculated largest SHG coefficient d_{eff} is 8.42 pm V^{-1} (0.73 eV), which promised such desirable NLO property for **2** (Fig. S5†). Birefringence calculations showed that the birefringence at the wavelength of 1.70 μm is 0.043 (Fig. 3d), respectively, which theoretically clarifies its phase-matchable behavior over a wide range.

Conclusions

In summary, based on the parent CS $[Cd_5P_2][SmCl_6]Cl$ (**1**), by applying the strategy of octahedral $[SmCl_6]^{3-}$ being substituted with acentric tetrahedral $[CdBr_4]^{2-}$ polyanion, the CS-to-NCS NLO supramolecule $[Cd_4P_2][CdBr_4]$ (**2**) can be obtained. The replacement also induces the host 2D–3D framework structural

transformation. Expectedly, the experimental and theoretical results indicate that compound **2** is a potential IR NLO material candidate with phase-matchable SHG effect ($0.8 \times$ AGS at 1.70 μm), band gap (2.37 eV), and thermal expansion coefficient anisotropy for high LIDT ($3.33 \times$ AGS at 2.09 μm). It is the first example that induces the CS-to-NCS structural transformation by polyanion substitution of a supramolecule, thereby opening a new avenue for designing functional materials based on NCS structure.

Experimental

Syntheses

Both compounds were synthesized by a solid-state reaction. A mixture of Sm powder (99.90%, Macklin, 1 mmol), P_{red} powder (98.50%, Macklin, 2 mmol), and $CdCl_2$ powder (99.99%, Aladdin, 5 mmol) for $[Cd_5P_2][SmCl_6]Cl$ (**1**), or Cd grains (99.99%, Macklin, 3 mmol), P_{red} powder (98.50%, Macklin, 2 mmol), and $CdBr_2$ powder (99%, Aladdin, 2 mmol) for $[Cd_4P_2][CdBr_4]$ (**2**), were weighed into silica tubes in an argon-filled glovebox. These tubes were vacuum-sealed and placed in a furnace and then heated to 773 K and 1073 K for **1** and **2**, respectively, at a rate of 30 K h^{-1}, and maintained at this temperature for 96 h, and then subsequently cooled to 573 K at a rate of 10 K h^{-1}. Afterwards, the furnaces were turned off. Semiquantitative microprobe chemical elemental analyses were conducted on a field emission scanning electron microscope (SU-8010) equipped with energy-dispersive X-ray spectroscopy to obtain information about the chemical composition of compounds **1** and **2**.

Single-crystal and powder XRD characterization

Single-crystal XRD was performed with a Rigaku FR-X Micro-focus diffractometer, using graphite monochromatic Mo-Kα radiation ($\lambda = 0.71073$ Å) at room temperature. The dataset integration and reduction were carried out using CrysAlisPro software.[50] The intensity data sets were collected with an ω-scan technique and reduced using the Siemens SHELXTL crystallography software package.[51] Then the anisotropic thermal parameters of all atoms were refined on F^2, employing the full-matrix least-squares techniques. Whether or not the symmetry of the final structures was reasonable was checked by the Addsym/Platon program.[52] The temperature-dependent lattice parameters of **2** were investigated at progressive temperatures ranging from 100 to 400 K. Moreover, the powder XRD data were collected at room temperature utilizing a MiniFlex 600 powder XRD equipped with Cu-Kα radiation ($\lambda = 1.54057$ Å) with 2θ ranging from 5° to 65° at a scan step width of 0.05°.

UV-vis-near infrared diffuse reflectance spectra

The UV-vis-NIR diffuse reflectance spectra of **1** and **2** were determined using a PerkinElmer Lambda 950 UV/Vis/NIR spectrophotometer, with a $BaSO_4$ plate as the benchmark in the wavelength range of 200–2500 nm at a rate of 284 nm min^{-1}.

SHG and LIDT measurements

The powder SHG signals of **2** and benchmark AGS that were obtained from optical-quality crystals were obtained using the modified Kurtz–Perry method using broadband wavelength from 1.06 to 1.70 μm. The samples **2** and AGS were finely ground and sieved into five distinct size ranges of 30–50, 50–75, 75–100, 100–125, 125–150, and 150–200 μm, which were placed and secured between the glass plates in a layer 0.1 mm thick. A charge-coupled device (CCD) camera equipped with nitrogen cooling was utilized to detect the signal. The LIDT measurements of single crystals **2** and AGS (set as reference) were carried out at the laser of 2.09 μm (10 ns, 1 Hz) until the damaged spot was found. The power of the progressively enhanced laser beam was investigated on a laser energy meter (Ophir Nova II). The formula $I_{(threshold)} = E/(\pi r^2 \tau_p)$ determined the damage threshold, where E, r, and τ_p are the laser damage energy of a single pulse, the radius of the spot, and the pulse width, respectively.

Computational methods

The band structure, density of states, and optical properties were calculated based on density functional theory (DFT) using the ABINIT software package. Exchange and correlation effects were treated by generalized gradient approximation. The following orbitals were regarded as valence electrons: P-$3s^2 3p^3$, Br-$3d^{10} 4s^2 4p^5$, and Cd-$4d^{10} 5s^2$. The k integration over the Brillouin zone was implemented by the tetrahedron method using $1 \times 1 \times 2$ Monkhorst–Pack κ-point meshes for primitive lattices.[53] The optical properties were calculated relying upon the complex dielectric function $\varepsilon_{ij} = \varepsilon_{ij,re}(\omega) + \varepsilon_{ij,im}(\omega)$, where $\varepsilon_{re}(\omega)$ and $\varepsilon_{im}(\omega)$ represent the real and imaginary parts of the dielectric function, respectively, which was given by $\frac{4\pi}{\Omega} \sum_{nmk} f_{nm}(k) \frac{r_{nm}^i(k) r_{nm}^j(k)}{\omega_{mn}(k) - \omega} + \delta_{ij}$ where $r_{nm}^i(k)$ is the position of matrix elements between states n and m. The frequency-dependent SHG susceptibility tensors χ_{ijk} (2ω, ω, ω) of compound **2** were computed using density functional perturbation theory and the "sum over states" method. The SHG susceptibility can be divided into three primary parts, the pure interband transition term χ_{inter} (2ω, ω, ω), the intraband transition term χ_{intra} (2ω, ω, ω), and the modulation term χ_{mod} (2ω, ω, ω).[54] The effective SHG coefficients were determined by the angular average effective NLO coefficient square $\langle d_{ijk}^2 \rangle$.[45]

Data availability

EDS, powder XRD patterns, IR and UV-vis-NIR spectrum, SHG coefficients, and LIDT results, crystallographic data, and additional figures and tables.

Author contributions

Z.-X. Qiu, B.-W. Liu and G.-C. Guo conceived the idea and wrote the manuscript. Z.-X. Zheng and X.-M. Jiang performed the theoretical calculations. Z.-X. Qiu performed the experiments.

All authors discussed the results and commented on the manuscript.

Conflicts of interest

There are no conflicts to declare.

Acknowledgements

References

1 V. Nguyen, B. Ji, K. Wu, B. Zhang and J. Wang, *Chem. Sci.*, 2022, **13**, 2640–2648.

2 J. Chen, C. Lin, X. Jiang, G. Yang, M. Luo, X. Zhao, B. Li, G. Peng, N. Ye, Z. Hu, J. Wang and Y. Wu, *Mater. Horiz.*, 2023, **10**, 2876–2882.

3 Y.-M. You, W.-Q. Liao, D. Zhao, H.-Y. Ye, Y. Zhang, Q. Zhou, X. Niu, J. Wang, P.-F. Li, D.-W. Fu, Z. Wang, S. Gao, K. Yang, J.-M. Liu, J. Li, Y. Yan and R.-G. Xiong, *Science*, 2017, **357**, 306–309.

4 X.-M. Jiang, S. Deng, M.-H. Whangbo and G.-C. Guo, *Natl. Sci. Rev.*, 2022, **9**, nwac017.

5 C. Wu, X. Jiang, L. Lin, Y. Hu, T. Wu, Z. Lin, Z. Huang, M. G. Humphrey and C. Zhang, *Angew. Chem., Int. Ed.*, 2021, **60**, 22447–22453.

6 F. You, F. Liang, Q. Huang, Z. Hu, Y. Wu and Z. Lin, *J. Am. Chem. Soc.*, 2018, **141**, 748–752.

7 J. Zhou, H. Wu, H. Yu, S. Jiang, Z. Hu, J. Wang, Y. Wu and P. S. Halasyamani, *J. Am. Chem. Soc.*, 2020, **142**, 4616–4620.

8 G. Zou, H. Jo, S.-J. Lim, T.-S. You and K. M. Ok, *Angew. Chem., Int. Ed.*, 2018, **57**, 8619–8622.

9 T. T. Tran, J. He, J. M. Rondinelli and P. S. Halasyamani, *J. Am. Chem. Soc.*, 2015, **137**, 10504–10507.

10 H. Liu, Y. Wang, B. Zhang, Z. Yang and S. Pan, *Chem. Sci.*, 2020, **11**, 694–698.

11 T. K. Bera, J.-H. Song, A. J. Freeman, J. I. Jang, J. B. Ketterson and M. G. Kanatzidis, *Angew. Chem., Int. Ed.*, 2008, **47**, 7828–7832.

12 X. Huang, S.-H. Yang, X.-H. Li, W. Liu and S.-P. Guo, *Angew. Chem., Int. Ed.*, 2022, **61**, e202206791.

13 J. A. Brant, D. J. Clark, Y. S. Kim, J. I. Jang, J.-H. Zhang and J. A. Aitken, *Chem. Mater.*, 2014, **26**, 3045–3048.

14 C. Li, W. Yin, P. Gong, X. Li, M. Zhou, A. Mar, Z. Lin, J. Yao, Y. Wu and C. Chen, *J. Am. Chem. Soc.*, 2016, **138**, 6135–6138.

15 H.-D. Yang, M.-Y. Ran, S.-H. Zhou, X.-T. Wu, H. Lin and Q.-L. Zhu, *Chem. Sci.*, 2022, **13**, 10725–10733.

16 J.-H. Zhang, S. S. Stoyko, A. J. Craig, P. Grima, J. W. Kotchey, J. I. Jang and J. A. Aitken, *Chem. Mater.*, 2020, **32**, 10045–10054.

17 J. Chen, L. Xiong, L. Chen and L.-M. Wu, *J. Am. Chem. Soc.*, 2018, **140**, 14082–14086.

18 B.-W. Liu, X.-M. Jiang, H.-Y. Zeng and G.-C. Guo, *J. Am. Chem. Soc.*, 2020, **142**, 10641–10645.

19 J. Chen, C. Lin, D. Zhao, M. Luo, G. Peng, B. Li, S. Yang, Y. Sun and N. Ye, *Angew. Chem., Int. Ed.*, 2020, **59**, 23549–23553.

20 M.-Y. Ran, A.-Y. Wang, W.-B. Wei, X.-T. Wu, H. Lin and Q.-L. Zhu, *Coord. Chem. Rev.*, 2023, **481**, 215059.

21 Q. Q. Liu, X. Liu, L. M. Wu and L. Chen, *Angew. Chem., Int. Ed.*, 2022, **134**, e202205587.

22 Y.-N. Li, Z.-X. Chen, W.-D. Yao, R.-L. Tang and S.-P. Guo, *J. Mater. Chem. C*, 2021, **9**, 8659–8665.

23 S. Cui, H. Wu, Z. Hu, J. Wang, Y. Wu and H. Yu, *Adv. Sci.*, 2023, **10**, 2204755.

24 W. Xing, F. Liang, C. Tang, E. Uykur, Z. Lin, J. Yao, W. Yin and B. Kang, *ACS Appl. Mater. Interfaces*, 2021, **13**, 37331–37338.

25 L. Luo, L. Wang, J. Chen, J. Zhou, Z. Yang, S. Pan and J. Li, *J. Am. Chem. Soc.*, 2022, **144**, 21916–21925.

26 J.-H. Zhang, D. J. Clark, J. A. Brant, K. A. Rosmus, P. Grima, J. W. Lekse, J. I. Jang and J. A. Aitken, *Chem. Mater.*, 2020, **32**, 8947–8955.

27 C. C. Stoumpos, L. Frazer, D. J. Clark, Y. S. Kim, S. H. Rhim, A. J. Freeman, J. B. Ketterson, J. I. Jang and M. G. Kanatzidis, *J. Am. Chem. Soc.*, 2015, **137**, 6804–6819.

28 X.-M. Jiang, M.-J. Zhang, H.-Y. Zeng, G.-C. Guo and J.-S. Huang, *J. Am. Chem. Soc.*, 2011, **133**, 3410–3418.

29 M. M. Shatruk, L. N. Reshetova, A. V. Shevel'kov and B. A. Popovkin, *Russ. J. Inorg. Chem.*, 2000, **45**, 495–499.

30 J. Galy, G. Meunier, S. Andersson and A. Åström, *J. Solid State Chem.*, 1975, **13**, 142–159.

31 C.-F. Sun, C.-L. Hu, X. Xu, B.-P. Yang and J.-G. Mao, *J. Am. Chem. Soc.*, 2011, **133**, 5561–5572.

32 G. Korum, *Reflectance Spectroscopy*, Springer, New York, 1969.

33 E. Buehler, J. Wernick and J. Wiley, *J. Electron. Mater.*, 1973, **2**, 445–454.

34 G. C. Catella and D. Burlage, *MRS Bull.*, 1998, **23**, 28–36.

35 X.-M. Jiang, G.-E. Wang, Z.-F. Liu, M.-J. Zhang and G.-C. Guo, *Inorg. Chem.*, 2013, **52**, 8865–8871.

36 X.-M. Jiang, X.-G. Li, Y.-H. Fan, B.-W. Liu, H.-Y. Zeng and G.-C. Guo, *Dalton Trans.*, 2013, **42**, 15475–15481.

37 S. J. Clark, M. D. Segall, C. J. Pickard, P. J. Hasnip, M. I. Probert, K. Refson and M. C. Payne, *Z. Kristallogr. – Cryst. Mater.*, 2005, **220**, 567–570.

38 M. C. Payne, M. P. Teter, D. C. Allan, T. Arias and J. D. Joannopoulos, *Rev. Mod. Phys.*, 1992, **64**, 1045–1097.

39 M.-J. Zhang, X.-M. Jiang, L.-J. Zhou and G.-C. Guo, *J. Mater. Chem. C*, 2013, **1**, 4754–4760.

40 M.-Y. Li, Z. Ma, B. Li, X.-T. Wu, H. Lin and Q.-L. Zhu, *Chem. Mater.*, 2020, **32**, 4331–4339.

41 X. Chen, H. Jo and K. M. Ok, *Angew. Chem., Int. Ed.*, 2020, **132**, 7584–7590.

42 J. Zhao, D. Mei, Y. Yang, W. Cao, C. Liu, Y. Wu and Z. Lin, *Inorg. Chem.*, 2019, **58**, 15029–15033.

43 J. Chen, C. Lin, G. Peng, F. Xu, M. Luo, S. Yang, S. Shi, Y. Sun, T. Yan and B. Li, *Chem. Mater.*, 2019, **31**, 10170–10177.

44 B. W. Liu, X. M. Jiang, B. X. Li, H. Y. Zeng and G. C. Guo, *Angew. Chem., Int. Ed.*, 2020, **59**, 4856–4859.

45 S. K. Kurtz and T. T. Perry, *J. Appl. Phys.*, 1968, **39**, 3798–3813.

46 H. Liu, Z. Song, H. Wu, Z. Hu, J. Wang, Y. Wu and H. Yu, *ACS Mater. Lett.*, 2022, **4**, 1593–1598.

47 Y. Song, S. Cui, Z. Qian, H. Yu, Z. Hu, J. Wang, Y. Wu and H. Wu, *Inorg. Chem. Front.*, 2022, **9**, 5932–5940.

48 S. P. Guo, Y. Chi and H. G. Xue, *Angew. Chem., Int. Ed.*, 2018, **130**, 11714–11717.

49 J. Xu, K. Wu, Y. Xiao, B. Zhang, H. Yu and H. Zhang, *ACS Appl. Mater. Interfaces*, 2022, **14**, 37967–37974.

50 R. O. Diffracion, *CrysAlisPRO Software System, Version 1.171. 39.32 a*, Rigaku Corporation, Oxford, UK, 2017.

51 G. Sheldrick, *SHELXL-97, Program for Crystal Structure Refinement*, 1997.

52 A. Spek, Single-crystal structure validation with the program PLATON, *J. Appl. Crystallogr.*, 2003, **36**, 7–13.

53 H. J. Monkhorst and J. D. Pack, *Phys. Rev. B: Solid State*, 1976, **13**, 5188–5192.

54 S. Sharma and C. A. Draxl, *Phys. Scr.*, 2004, **109**, 128–134.